Title

Self-Assembled Magnetic Nanoparticle Layers: Structural Control for Reconfigurable Magnetism and Functional Applications

Permalink

https://escholarship.org/uc/item/9676g1x5

Journal

ACS Applied Nano Materials, 8(13)

ISSN

2574-0970

Authors

Lu, Xingyuan
Zou, Ji
Pham, Minh
et al.

Publication Date

2025-04-04

DOI

10.1021/acsanm.5c00461

Self-Assembled Magnetic Nanoparticle Layers: Structural Control for Reconfigurable Magnetism and Functional Applications

Xingyuan Lu[1,2†], Ji Zou[1,3†], Minh Pham[1,4], Arjun Rana[1], Chen-Ting Liao[5], Emma Cating Subramanian[5], Xuefei Wu[6], Yuan Hung Lo[1], Charles S. Bevis[5], Robert M. Karl[5], Serban Lepadatu[7], Young-Sang Yu[8], Yaroslav Tserkovnyak[1], Thomas P. Russell[6], David A. Shapiro[8], Henry Kapteyn[5], Margaret Murnane[5], Robert Streubel[9] and Jianwei Miao[1]*

[1]Department of Physics & Astronomy and California NanoSystems Institute, University of California, Los Angeles, CA 90095, USA and STROBE Science and Technology Center

[2]School of Physical Science and Technology, Soochow University, Suzhou 215006, China

[3]Department of Physics, University of Basel, Klingelbergstrasse 82, CH-4056 Basel, Switzerland

[4]Department of Mathematics, University of California, Los Angeles, CA 90095, USA and STROBE Science and Technology Center

[5]JILA and Department of Physics, University of Colorado and NIST, 440 UCB, Boulder, Colorado 80309, USA and STROBE Science and Technology Center

[6]Polymer Science and Engineering Department University of Massachusetts, Amherst, Massachusetts 01003, USA

[7]Jeremiah Horrocks Institute for Mathematics, Physics and Astronomy, University of Central Lancashire, Preston, PR1 2HE, U.K.

[8]Advanced Light Source, Lawrence Berkeley National Laboratory, Berkeley, CA 94720, USA

[9]Department of Physics & Astronomy, University of Nebraska-Lincoln, Lincoln, NE 68588, USA

ABSTRACT: We advance soft X-ray vector ptychographic tomography to map the 3D magnetization field in self-assembled superparamagnetic nanoparticles at a liquid-liquid interface, revealing how layered structures influence magnetic ordering. We observe that monolayers with low coordination numbers exhibit weak magnetic order, with magnetic vortices disrupting spin alignment. In contrast, bilayers and trilayers with higher coordination numbers display long-range magnetic order, with strong spin correlations across larger distances and a suppression of magnetic vortices. We further quantify the average distance for vortex-antivortex pairs as 26.0 ± 2.0 nm, while vortex-vortex and antivortex-antivortex pairs exhibit larger separations, averaging 44.9 ± 5.2 nm and 54.1 ± 7.4 nm, respectively. These experimental results are supported by micromagnetic Monte Carlo simulations. Our findings illustrate how layered structures enhance magnetic order and spin correlation in superparamagnetic nanoparticle assemblies, providing a promising approach for tuning magnetic properties in applications such as data storage, microrobotics, and biomedicine.

KEYWORDS: *Nanoparticles, Magnetic order, X-ray ptychography, Vector tomography, Magnetic topology*

1. INTRODUCTION

Magnetic nanostructures [1–3] have been used in commercial, biomedical, and research applications for many decades, typically as individual superparamagnetic iron oxide nanoparticles dispersed in a solution or as ferromagnetic agglomerates. Recent advances in synthesis capabilities and physical understanding enabled the creation of reconfigurable ferromagnetic liquid droplets for microrobotics by mechanical jamming of magnetic nanoparticles at liquid-liquid interfaces [4–9], smart hydrogels [10] for continuous health monitoring, high-frequency electronics [11], and organic multiferroic materials for molecular microelectronics [12,13]. In either case, the translational and rotational degrees of freedom of the disordered nanoparticles are restricted and the magnetic order-by-disorder phenomenon [14] governs the transition between superparamagnetism and collective behavior, e.g., spin glass, macrovortex phases [15], and superferromagnetism [16], and, hence, the functionality of the composite materials.

Lacking experimental capabilities, superparamagnetic nanoparticles have been approximated as uniformly magnetized objects neglecting a slightly more complex inner structure [17]. The random on-site interaction of disordered assemblies depends on the symmetry [18], spacing [19], and disorder [20] that can enhance remanent magnetization and coercive field [21] or lift the continuous degeneracy of frustrated systems to a discrete symmetry resembling the underlying structure [22]. Both interaction strength and collective behavior, such as spin glass character [16,23], associated with magnetic interparticle coupling are typically deduced from field/zero-field cooling experiments [16], magnetization relaxation using the Néel-Brown [24-26] or the Vogel-Fulcher-Tammann [27-29] theory, or first-order reversal curves [30] and correlated with the structural short-range order inferred from, e.g., transmission electron microscopy. However, the inhomogeneity of nanoparticle assemblies prevents establishing a quantitative relationship between coordination and prevailing magnetization configuration.

Here, we image the 3D magnetization vector field in self-assembled superparamagnetic iron oxide nanoparticles leveraging X-ray vector ptychographic tomography [31-34], an advanced coherent diffractive imaging technique [35]. Most nanoparticles exhibit a uniformly magnetized state (macrospin) of varying time-averaged magnitude associated with superparamagnetism. Quantitative analysis reveals a strong influence of the coordination and magnetostatic environment on the macrospin collinearity and the formation of local macrovortices. Multilayer regions with larger coordination numbers show fewer macrovortices and better spin alignment consistent with the transition from spin glass to superferromagnetism.

2. EXPERIMENTAL SECTION

Our experiment involved functionalized superparamagnetic Fe_3O_4 nanoparticles with a magnetic core of approximately 22 nm, surrounded by electrostatically charged ligands to prevent agglomeration [4-6]. The sample was prepared by drop-casting aqueous nanoparticle dispersions onto silicon nitride membranes, which were then dried under ambient conditions (Figure S1). In the densely packed assembly, the jammed nanoparticles remain fixed, suppressing any mechanical rotation or translation. The experiment was conducted at the COSMIC beamline at the Advanced Light Source (Berkeley, CA), where circularly polarized X-rays, tuned to 713 eV (near the Fe_3O_4 L_3 edge and with an absorption peak in absorption spectroscopy, see Supporting Information Figure S2) [36], were focused onto the sample using a zone plate (Figure 1). For 3D vector reconstruction, two tilt series were acquired at in-plane rotation angles of 0° and 120°. At each in-plane angle, the sample was rotated about the x-axis, generating a tilt series of coherent x-ray diffraction patterns. For each tilt, the focused beam was raster-scanned across the sample, and two diffraction pattern sets were collected with left- and right-circularly polarized X-rays (Table S1). The full dataset contained 213,996 diffraction patterns, from which 70 images were reconstructed via the ptychographic iterative engine algorithm [37]. After normalization, background subtraction, and alignment using the center of mass method [38], each pair of oppositely polarized images was summed to create 35 projections for 3D scalar reconstruction.

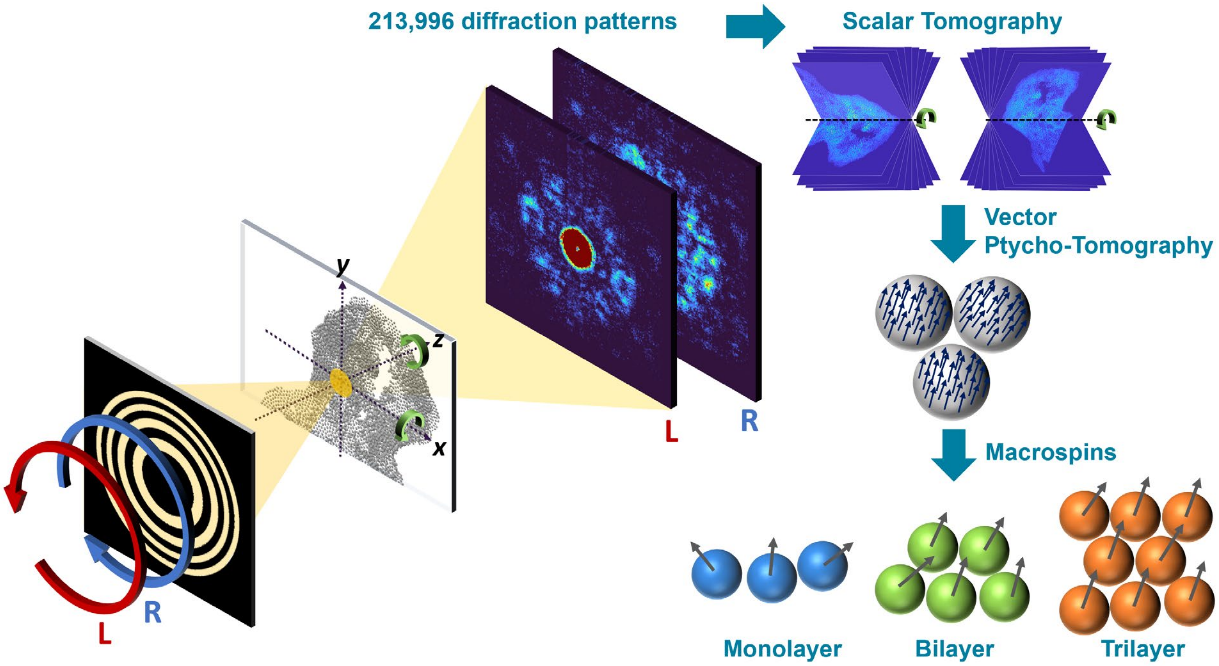

Figure 1. Schematic of soft X-ray vector ptychographic tomography. X-rays with a photon energy of 713 eV were focused onto the magnetic sample using a zone plate. The sample, composed of functionalized superparamagnetic Fe_3O_4 nanoparticles, was prepared by drop-casting aqueous nanoparticle dispersions onto silicon nitride membranes. During the experiment, the sample was rotated around the x- and z-axes, while the focused beam raster-scanned the sample at each angle, capturing diffraction patterns using left- and right-circularly polarized X-rays. These diffraction patterns were then utilized to reconstruct the 3D magnetization field in the self-assembled nanoparticles.

3. RESULTS AND DISCUSSION

Scalar tomography was conducted using Real Space Iterative Reconstruction (RESIRE), an advanced algorithm that enables 3D reconstruction from limited projections with automated angular refinement [39,40] (Supporting Information). A resolution estimation is shown in Figure S3. Figures 2a–d and S4 show the 3D scalar reconstruction of the nanoparticle assembly (grey regions), revealing monolayers, bilayers, and trilayers. From this reconstruction, we traced the 3D coordinates of the nanoparticles to calculate the radial distribution function, which indicates short-range structural order with a peak at 32.5 nm (Figure S5). Differences between left- and right-circularly polarized images, taken under identical conditions, produced 35 projections for 3D vector reconstruction (Figure S6). The magnetization vector field was then reconstructed using a vector tomography method [33,41], with a 3D support derived from the scalar reconstruction (Supporting Information). Given the sample's maximum of three layers, these 35 projections were sufficient for accurate scalar and vector reconstructions.

Quantitative analysis of the magnetic order in the nanoparticle assembly was conducted by examining the net magnetization, or macrospin, within each nanoparticle, based on the 3D vector reconstruction (Figure 2a). Figures 2b–d illustrate macrospin distributions in monolayer, bilayer, and trilayer regions, revealing that macrospin magnitude increases with the number of layers. This trend is attributed to varying microspin collinearity within each nanoparticle, as shown in Figure S7a-c. We found a positive correlation between microspin collinearity and coordination number (Figure S7d): nanoparticles with higher coordination numbers, such as those in trilayer regions, exhibit greater collinearity and thus larger macrospins. Here, coordination number is defined as the number of neighboring nanoparticles within a 54 nm radius that less than the next-nearest neighbor distance (Figure S5). Collinearity in Figure S7d is quantified by $\mathbf{m} \cdot \bar{\mathbf{m}}$, ranging from -1 (reverse collinearity) to +1 (complete collinearity), where $\mathbf{m}$ represents the microspin within the nanoparticle and $\bar{\mathbf{m}}$ the average normalized microspin. Figures 2e and f display histograms of the macrospin magnitude and angle, where the angle is defined as $\cos\theta = \boldsymbol{S} \cdot \bar{\boldsymbol{S}}$, with $\boldsymbol{S}$ representing the normalized macrospin and $\bar{\boldsymbol{S}}$ the overall average macrospin. The mean and standard deviations of the macrospin magnitudes are 0.17 ± 0.10 (monolayer), 0.25 ± 0.12 (bilayer), and 0.33 ± 0.15 (trilayer) (Figure S7e), indicating increasing collinearity with the number of layers.

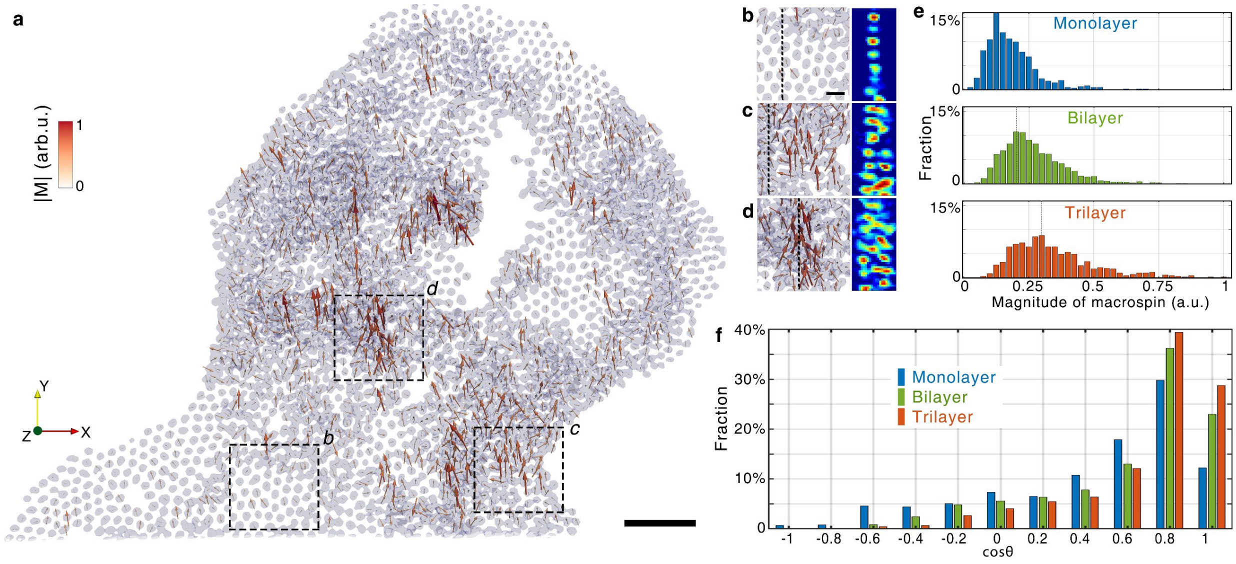

Figure 2. Observation of magnetic order in self-assembled Fe_3O_4 nanoparticles. (a) 3D scalar and vector reconstruction of the magnetic nanoparticle assembly, showing the 3D magnetization field within each nanoparticle as a macrospin (represented by arrows). (b-d) Zoomed-in views of the boxed regions in (a) and corresponding cross sections (at dashed black lines), highlighting a monolayer (b), bilayer (c), and trilayer (d) region. The color bar in (a) indicates macrospin magnitude for (a-d). (e, f) Histograms of macrospin magnitude and angle across monolayer, bilayer, and trilayer regions. Scale bars: 200 nm in (a) and 50 nm in (b).

The formation of magnetic vortices and anti-vortices in the nanoparticle assembly plays a crucial role in establishing magnetic order [42]. The planar vortex profile of spins in the xy plane is typically characterized by the winding number of the polar angle. This vorticity concept can be extended to a continuum of Heisenberg spins and quantified as vortex density [43],

$$\rho(x,y) = \frac{1}{\pi}\hat{\boldsymbol{z}} \cdot \left(\partial_x \boldsymbol{S} \times \partial_y \boldsymbol{S}\right). \qquad (1)$$

The total vortex number within an area Ω is given by,

$$Q = \int_{\Omega} \rho \, dxdy = \frac{1}{2\pi}\int_{\partial\Omega} \boldsymbol{S}_{||}^2 \, \nabla\varphi \cdot d\boldsymbol{l}, \qquad (2)$$

where $\boldsymbol{S}_{||} = (S^x, S^y)$ denotes the planar projection of the vector field $\boldsymbol{S}$, φ is its polar angle relative to the x-axis, and $\partial\Omega$ represents the boundary of the area parameterized by $\boldsymbol{dl}$. This vorticity definition in Eqs. (1) and (2) incorporates the 3D nature of the Heisenberg spin vector field, unlike the traditional winding number. When the vector field is purely in-plane with a vanishing z-component, this vorticity simplifies to the conventional winding number. Moreover, it preserves the topological properties of vorticity, as described by the bulk-edge correspondence in Eq. (2): the vortex number within a region remains constant under vector field deformations, provided the boundary field is fixed.

To determine the vortex number for a triangular region defined by three vertices, we discretize Eq. (1) as,

$$\rho = \frac{\hat{\boldsymbol{z}} \cdot \sum_{<l,l'>} (\boldsymbol{S}_l \times \boldsymbol{S}_{l'})}{2\pi}, \qquad (3)$$

where $\hat{\boldsymbol{z}}$ is the normal vector to the triangular plane, $\boldsymbol{S}$ is the normalized macrospin at each vertex, and the sum runs over the three edges (l' is the vertex adjacent to l in the counterclockwise direction). Since triangles form the basis of arbitrary 2D lattices, Eq. (3) applies to our nanoparticle assembly with short-range structural order [44]. Summing vortex contributions from all triangles yields the total vortex charge within a region, which vanishes in the bulk, leaving only boundary terms. This establishes a discrete bulk-edge correspondence for vortices [44], where the vortex number per triangle is not strictly quantized (Supporting Information).

Figure 3a shows the distribution of typical magnetic vortices and anti-vortices with $|\rho| \geq 0.25$, and a detailed vortex density map is provided in Figure S8a. Figures 3b–d illustrate typical configurations, including collinear and anti-aligned vortex arrangements. Vortex density is negatively correlated with coordination number (Figure 3e and Figure S9), with higher densities in monolayers (low coordination number, A1 in Figure 3a) and suppressed in trilayers (high coordination number, A2 in Figure 3a). The vortices at the transition boundaries, named as "border vortex", was also identified based on whether the three nanoparticles forming the vortex are located in different regimes. For example, one nanoparticle resides in the monolayer region while the other two are in the bilayer region. Through this analysis, we found a total of 25 border vortices (13 antivortices and 12 vortices). The proportion of border vortices to the total possible triangles formed by nanoparticles at the boundaries is 0.52%. For comparison, the number of vortices and corresponding proportion in monolayer (20, 3.25%), bilayer (27, 0.46%), and trilayer (6, 0.25%) regions was also quantified, as shown in Figure 3f. It shows that vortex formation is more likely to occur in monolayer and at the boundaries. Moreover, it was observed that most of the border vortices are located at the boundaries between monolayer and bilayer regions (22 out of 25), further highlighting that higher coordination numbers suppress vortex formation, also at the boundaries.

Analysis of vortex-antivortex (Figure 3g), vortex-vortex (Figure 3h), and antivortex-antivortex distances (Figure 3i) shows a tendency for vortices and antivortices to attract. Vortex-antivortex pairs have an average distance of 26.0 ± 2.0 nm, following a generalized extreme value distribution. Vortex-vortex and antivortex-antivortex distances are larger, at 44.9 ± 5.2 nm and 54.1 ± 7.4 nm, respectively, indicating distinct interactions based on vortex charge, contributing to a vortex screening effect. Each dot in Figure 3a represents a nanoparticle, while each dot in Figure S8a marks the center of a triangle of three nanoparticles. Vortex size, defined by the circumcircle diameter of each triangle, averages 59.4 ± 4.0 nm, and vortex separation is measured as the distance between triangle centers in Figure S8a, allowing vortex distances to be smaller than their sizes (Supporting Information).

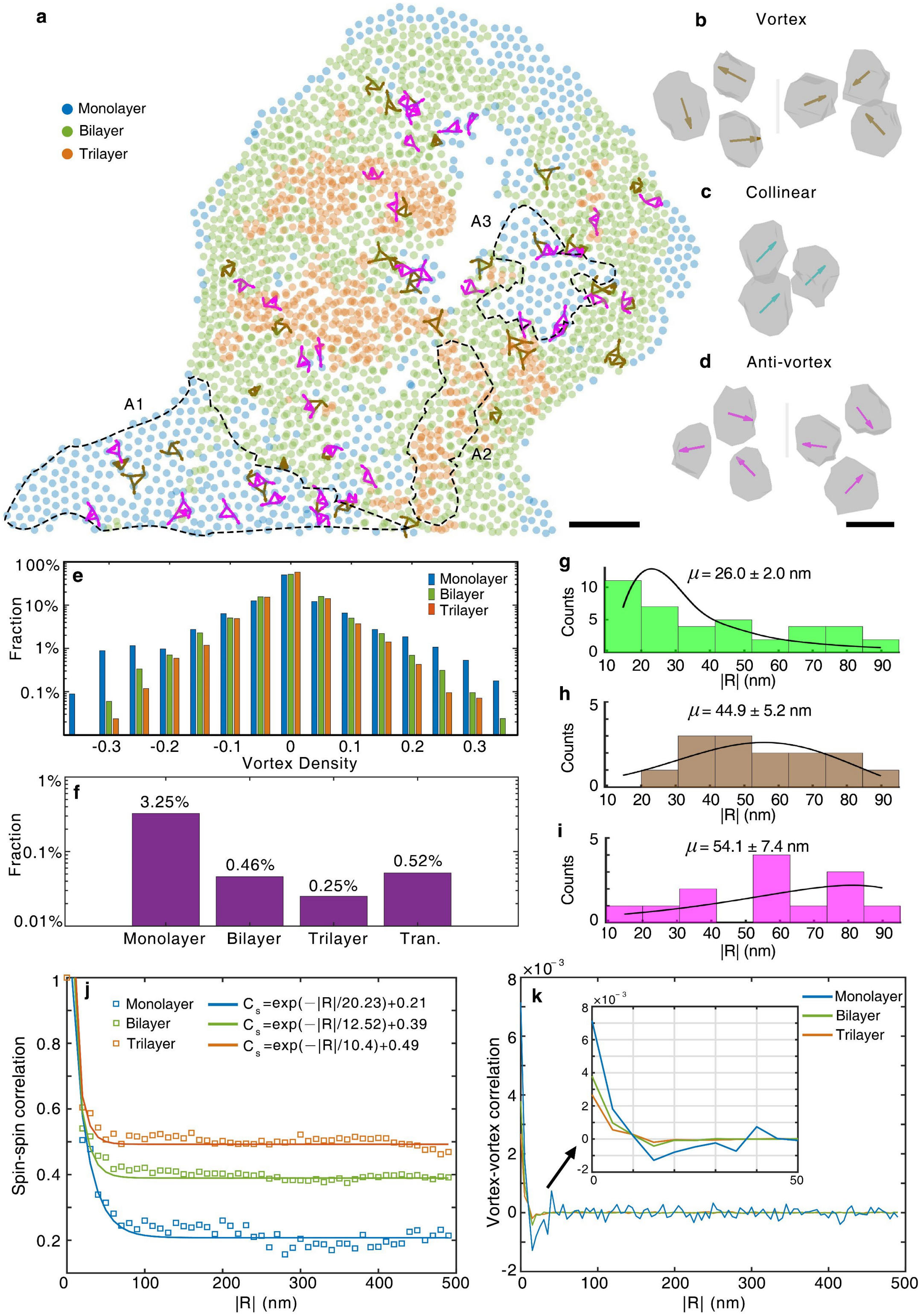

Figure 3. Quantitative demonstration that magnetic vortices and anti-vortices dominate in monolayer regions, while they are much suppressed in bilayer and trilayer regions, that exhibit stronger spin and macro

spin alignment. (a) Distribution of magnetic vortices (brown triangles) and anti-vortices (pink triangles) in the nanoparticle assembly. Blue, green, and orange circles represent nanoparticles in monolayer, bilayer, and trilayer regions, respectively. Areas A1, A2, and A3 (dashed outlines) highlight: a monolayer region with numerous vortices/anti-vortices, a trilayer region lacking vortices, and a boundary region with abundant vortices, respectively. (b–d) Enlarged views of two representative vortices (b), collinear spins (c), and two anti-vortices (d). (e) Vortex density histogram across monolayer, bilayer, and trilayer regions (normalized to 1 per region). (f) Proportion of magnetic vortices shown in panel a for monolayer (M), bilayer (B), trilayer (T), and transition boundary (Tran.). The y axis is in log scale. (g–i) Nearest-neighbor distances for vortex-antivortex (g), vortex-vortex (h), and anti-vortex-anti-vortex pairs (i). (j, k) Spin-spin (j) and vortex-vortex correlation functions (k) in each layer. Scale bars: 200 nm (a), 30 nm (d).

The magnetic order in different regions was analyzed using the spin-spin correlation function, $C_{spin}(|\boldsymbol{R}|) = \langle \boldsymbol{S}(\boldsymbol{r})\boldsymbol{S}(\boldsymbol{r}+\boldsymbol{R})\rangle_{\boldsymbol{r}}$, where $|\boldsymbol{R}|$ is the pair distance. In the monolayer (blue curve in Figure 3j), the correlation function decays exponentially, reaching ~0.21 at large distances with a correlation length of $\xi \approx 20$ nm, indicating weak spin alignment. This correlation length is comparable to the nanoparticle size, suggesting minimal collinearity even between nearest macrospins (Figure S5). In contrast, the bilayer and trilayer correlation functions (green and orange curves in Figure 3j) saturate at higher values (~0.4 and ~0.5) beyond 500 nm, indicating magnetic long-range order and stronger spin alignment. These results align with our observations of a higher density of vortices and antivortices in monolayers compared to bilayers and trilayers.

We further validated these findings by analyzing the vortex correlation function, $C_{vortex}(|\boldsymbol{R}|) = \langle \rho(\boldsymbol{r})\rho(\boldsymbol{r}+\boldsymbol{R})\rangle_{\boldsymbol{r}}$. Figure 3k displays the correlation functions for monolayer (blue), bilayer (green), and trilayer (orange) regions. At $|\boldsymbol{R}| = 0$, the positive correlation reflects the average squared density of vortices, with the monolayer showing the highest density $C_{vortex}(0) = 7.2 \times 10^{-3}$. This high vortex density disrupts long-range magnetic order, in contrast to the lower values observed in the bilayer (4×10^{-3}) and trilayer (2.9×10^{-3}). The vortex correlation functions decrease to negative values at short distances before decaying to zero (Figure 3k), indicating that vortices with opposite charges tend to cluster together, consistent with the small average distance between vortex-antivortex pairs. This screening effect leads to zero correlation at larger distances. In the monolayer, the correlation shows greater fluctuations around zero at large distances than in the bilayer and trilayer, primarily due to positioning noise. The bilayer and trilayer, with fewer vortices, naturally exhibit lower noise in their correlation functions.

To validate the reconstructed magnetization vector field and magnetic correlations, we compared them with magnetic simulations, linking structural short-range order to magnetic ordering. Using the experimentally determined 3D coordinates as input, we modeled the magnetic nanoparticle assembly at 300 K through micromagnetic Monte Carlo simulations with Boris Spintronics [45,46] (Supporting Information). Each nanoparticle was treated as a macrospin with variable magnetization length, interacting via dipolar fields. The magnetic hysteresis loop displayed a small remanence value (Figure 4a), and the magnetization length distribution matched the expected Maxwell-Boltzmann distribution with a mean near the saturation magnetization [45, 47]. Considering all three regions, the spin-spin (Figure 4b) and vortex-vortex correlation functions (Figure 4c) from the simulations aligned well with experimental trends, particularly in the vortex density distribution. Both experimental (Figures 3f and S8a) and simulated (Figures S8b and S6) data show a higher vortex and anti-vortex density in monolayers than in bilayers and trilayers, with increased vortex formation at layer boundaries (Figure 4d), consistent with dipolar-induced spin frustration.

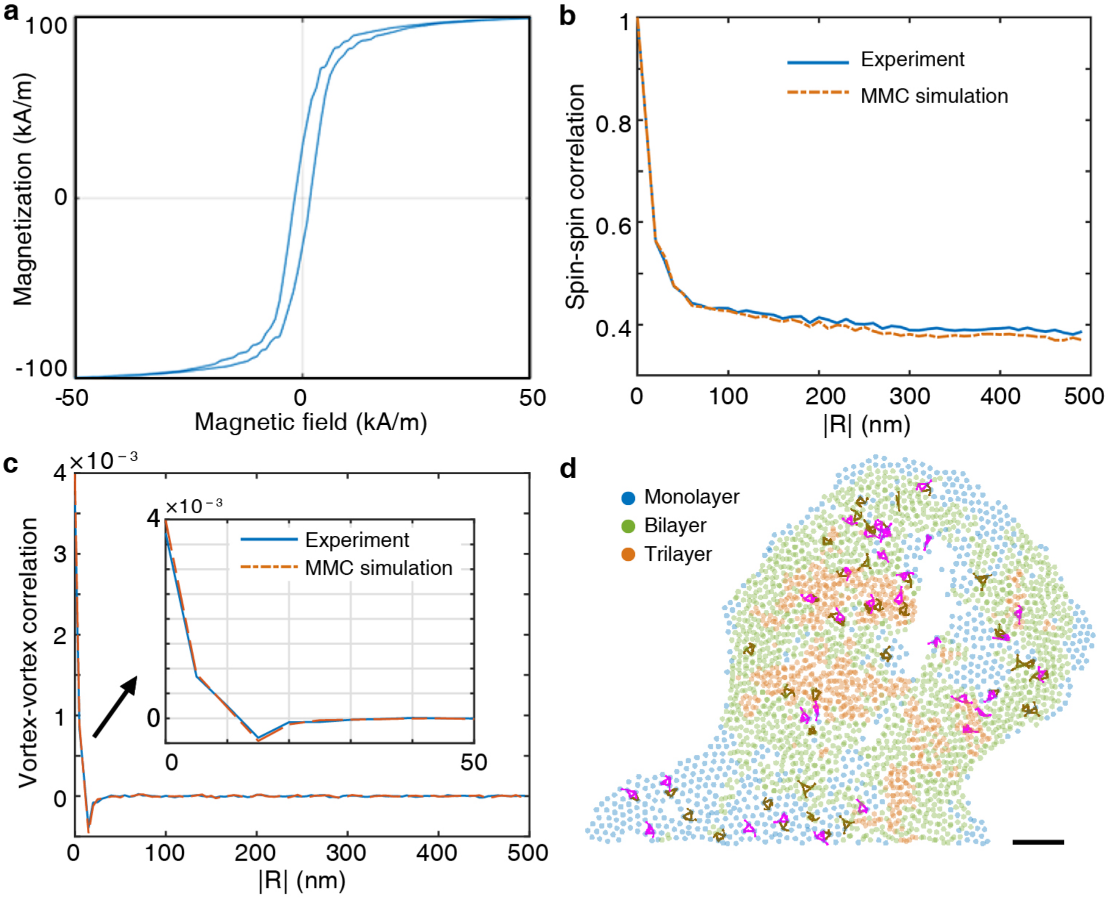

Figure 4. Micromagnetic Monte Carlo simulations using the experimentally derived 3D coordinates and macrospin configurations of magnetic nanoparticles. (a) In-plane magnetic hysteresis loop with a Curie temperature T_c = 850 K, indicating weak ferromagnetism. (b) Spin-spin correlation function and (c) vortex-vortex correlation function, both showing trends consistent with experimental observations. All three regions have been taken into account. (d) Distribution of magnetic vortices (brown triangles) and antivortices (pink triangles), with blue, green, and orange circles representing nanoparticles in monolayer, bilayer, and trilayer regions, respectively. Scale bar: 200 nm

4. CONCLUSIONS

In conclusion, soft X-ray vector-ptychographic tomography unveiled the 3D magnetization vector field and magnetic order in Fe_3O_4 nanoparticle assemblies at room temperature. Our findings demonstrate that magnetization stability and configuration within each nanoparticle depend on the layered structure and coordination number. Increasing the number of layers enhances net magnetization due to greater spin alignment within nanoparticles with larger coordination numbers. Spin-spin and vortex-vortex correlation analyses revealed long-range macrospin order in bilayer and trilayer regions, along with magnetic vortices and anti-vortices in monolayer regions and at interlayer boundaries. The measured distance between vortex-antivortex pairs was 26.0 ± 2.0 nm, compared to larger separations of 44.9 ± 5.2 nm and 54.1 ± 7.4 nm for vortex-vortex and antivortex-antivortex pairs, respectively. Micromagnetic Monte Carlo simulations based on experimental 3D coordinates validate our observations, highlighting the crucial role of layered structures in shaping nanoparticle magnetization.

ASSOCIATED CONTENT

Supporting Information. Further information on sample preparation, data acquisition, ptychographic and 3D scalar reconstructions, spatial resolution estimation, 3D vector reconstruction, data analysis, vorticity calculations for Heisenberg macrospins on a lattice, vortex spacing, and micromagnetic Monte Carlo simulations.

AUTHOR INFORMATION

Corresponding Author

*Email: j.miao@ucla.edu

Author Contributions

J.M. directed the project. X.W. and T.P.R. prepared the sample. A.R., C.-T.L., Y.H.L., E.C.S., C.S.B., R.M.K., S.L., X.L., Y.-S.Y., D.A.S., H.C.K., M.M.M., and J.M. contributed to the planning and/or execution of the experiments. X.L., M.P., and J.M. performed the 3D scalar and vector reconstructions, while S.L. and R.S. conducted the Monte Carlo simulations. X.L., J.Z., R.S., Y.T., and J.M. analyzed the data. X.L., J.Z., R.S., and J.M. wrote the manuscript, with contributions from M.M.M., Y.T. and T.P.R.

†These authors contributed equally to this work.

ACKNOWLEDGMENT

This work was supported by STROBE, a National Science Foundation Science and Technology Center (award DMR1548924), and the U.S. Air Force Office Multidisciplinary University Research Initiative (MURI) program (award FA9550-23-1-0281). R.S. received support from the NSF Division of Materials Research (grant 2203933). The soft X-ray vector-ptychographic tomography experiments were conducted at COSMIC using resources at the Advanced Light Source, a U.S. Department of Energy Office of Science User Facility (contract DE-AC02-05CH11231). M.M. and H.K. acknowledge partial support for personnel by the US Department of Energy, Office of Science, Basic Energy Sciences X-Ray Scattering Program Award DE-SC0002002. X.W. and T.P.R. were supported by the DOE Office of Science, Basic Energy Sciences, Materials Sciences and Engineering Division (contract DE-AC02-05CH11231) through the Adaptive Interfacial Assemblies Towards Structuring Liquids program (KCTR16).

REFERENCES

[1] Fernandez-Pacheco, A.; Streubel, R.; Fruchart, O.; Hertel, R.; Fischer, P.; Cowburn, R. P. Three-dimensional nanomagnetism. *Nat. Commun.* **2017**, 8, 15756.

[2] Streubel, R.; Tsymbal, E. Y.; Fischer, P. Magnetism in curved geometries. *J. Appl. Phys.* **2021**, 129, 210902.

[3] Gubbiotti, G.; Barman, A.; Ladak, S.; Bran, C.; Grundler, D.; Huth, M.; Plank, H.; Schmidt, G.; Dijken, S.; Streubel, R.; Dobrovoloskiy, O.; Scagnoli, V.; Heyderman, L.; Donnelly, C.; Hellwig, O.; Fallarino, L.; Jungfleisch, M. B.; Farhan, A.; Maccaferri, N.; Vavassori, P.; Fischer, P.; Tomasello, R.; Finocchio, G.; Clérac, R.; Sessoli, R.; Makarov, D.; Sheka, D. D.; Krawczyk, M.; Gallardo, R.; Landeros, P.; d'Aquino, M.; Hertel, M.; Pirro, P.; Ciubotaru, F.; Becherer, M.; Gartside, J.; Ono, T.; Bortolotti, P.; Fernández-Pacheco, A. 2025 Roadmap on 3D Nano-magnetism. *J. Phys.: Condens. Matter* **2024**.

[4] Liu, X.; Kent, N.; Ceballos, A.; Streubel, R.; Jiang, Y.; Chai, Y.; Kim, P. Y.; Forth, J.; Hellman, F.; Shi, S. Reconfigurable ferromagnetic liquid droplets. *Science* **2019**, 365 (6450), 264-267.

[5] Streubel, R.; Liu, X.; Wu, X.; Russell, T. P. Perspective: Ferromagnetic Liquids. *Materials* **2020**, 13 (12), 2712.

[6] Wu, X.; Streubel, R.; Liu, X.; Kim, P. Y.; Chai, Y.; Hu, Q.; Wang, D.; Fischer, P.; Russell, T. P. Ferromagnetic liquid droplets with adjustable magnetic properties. *Proc. Natl. Acad. Sci. USA* **2021**, 118 (8), e2017355118.

[7] Liu, X.; Tian, Y.; Jiang, L. Manipulating dispersions of magnetic nanoparticles. *Nano Lett.* **2021**, 21, 2699.

[8] Wu, X.; Bordia, G.; Streubel, R.; Hasnain, J.; Pedroso, C. C. S.; Cohen, B. E.; Rad, B.; Ashby, P.; Omar, A. K.; Geissler, P. L.; Wang, D.; Xue, H.; Wang, J.; Russell, T. P. Ballistic Ejection of Microdroplets from Overpacked Interfacial Assemblies. *Adv. Funct. Mater.* **2023**, 33, 2213844.

[9] Wu, X.; Xue, H.; Bordia, G.; Fink, Z.; Kim, P. Y.; Streubel, R.; Han, J.; Helms, B. A.; Ashby, P. D.; Omar, A. K.; Russell, T. P. Self-Propulsion by Directed Explosive Emulsification. *Adv. Mater.* **2024**, 36 2310435.

[10] Beebe, D. J.; Moore, J. S.; Bauer, J. M.; Yu, Q.; Liu, R. H.; Devadoss, C.; Jo, B. H. Functional hydrogel structures for autonomous flow control inside microfluidic channels. *Nature* **2000**, 404(6778), 588-590.

[11] Bavatharani, C.; Muthusankar, E.; Wabaidur, S. M.; Alothman, Z. A.; Alsheetan, K. M.; mana AL-Anazy, M.; Ragupathy, D. Electrospinning technique for production of polyaniline nanocomposites/nanofibres for multi-functional applications: A review. *Synth. Met.* **2021**, 271, 116609.

[12] Ben Dor, O.; Yochelis, S.; Radko, A.; Vankayala, K.; Capua, E.; Capua, A.; Yang, S. H.; Baczewski, L. T.; Parkin, S. S. P.; Naaman, R.; Paltiel, Y. Magnetization switching in ferromagnets by adsorbed chiral molecules without current or external magnetic field. *Nat. Commun.* **2017**, 8(1), 14567.

[13] Fransson, J. Charge redistribution and spin polarization driven by correlation induced electron exchange in chiral molecules. *Nano Lett.* **2021**, 21(7), 3026-3032.

[14] Prakash, S.; Henley, C. L. Ordering due to disorder in dipolar magnets on two-dimensional lattices. *Phys. Rev. B* **1990**, 42(10), 6574.

[15] Streubel, R.; Kent, N.; Dhuey, S.; Scholl, A.; Kevan, S.; Fischer, P. Spatial and temporal correlations of XY macro spins. *Nano Lett.* **2018**, 18(12), 7428-7434.

[16] Bedanta, S.; Kleemann, W. Supermagnetism. *J. Phys. D: Appl. Phys.* **2008**, 42(1), 013001.

[17] Krycka, K. L. Booth, R. A.; Hogg, C. R.; Ijiri, Y.; Borchers, J. A.; Chen, W. C.; Watson, S. M.; Laver, M.; Gentile, T. R.; Dedon, L. R.; Harris, S.; Rhyne, J. J.; Majetich, S. A. Core-

shell magnetic morphology of structurally uniform magnetite nanoparticles. *Phys. Rev. Lett.* **2010**, 104(20), 207203.

[18] Luttinger, J. M.; Tisza, L. Theory of dipole interaction in crystals. *Phys. Rev.* **1946**, 70(11-12), 954.

[19] Leo, N.; Holenstein, S.; Schildknecht, D.; Sendetskyi, O.; Luetkens, H.; Derlet, P. M.; Scagnoli, V.; Lançon, D.; Mardegan, J. R. L.; Prokscha, T.; Suter, A.; Salman, Z.; Lee, S.; Heyderman, L. J. Collective magnetism in an artificial 2D XY spin system. *Nat. Commun.* **2018**, 9(1), 2850.

[20] Gallina, D.; Pastor, G. M. Disorder-induced transformation of the energy landscapes and magnetization dynamics in two-dimensional ensembles of dipole-coupled magnetic nanoparticles. *Phys. Rev. X* **2020**, 10(2), 021068.

[21] Kasyutich, O.; Desautels, R. D.; Southern, B. W.; Van Lierop, J. Novel aspects of magnetic interactions in a macroscopic 3D nanoparticle-based crystal. *Phys. Rev. Lett.* **2010**, 104(12), 127205.

[22] De'Bell, K.; MacIsaac, A. B.; Whitehead, J. P. Dipolar effects in magnetic thin films and quasi-two-dimensional systems. *Rev. Mod. Phys.* **2000**, 72(1), 225.

[23] Hohenberg, P. C.; Halperin, B. I. Theory of dynamic critical phenomena. *Rev. Mod. Phys.* **1977**, 49(3), 435.

[24] Néel, L. Théorie du traînage magnétique des ferromagnétiques en grains fins avec application aux terres cuites. *Ann. Géophys.* **1949**, Vol. 5, pp. 99-136.

[25] Brown Jr W. F. Thermal fluctuations of a single-domain particle. *Phys. Rev.* **1963**, *130*(5), 1677.

[26] Wernsdorfer, W.; Orozco, E. B.; Hasselbach, K.; Benoit, A.; Barbara, B.; Demoncy, N.; Mailly, D. Experimental evidence of the Néel-Brown model of magnetization reversal. *Phys. Rev. Lett.* **1997**, *78*(9), 1791.

[27] Vogel, H. Das temperaturabhangigkeitsgesetz der viskositat von flussigkeiten. *Phys. Z.* **1921**, *22*, 645-646.

[28] Fulcher, G. S. Analysis of recent measurements of the viscosity of glasses. *J. Am. Ceram. Soc.* **1925**, *8*(6), 339-355.

[29] Stock, A. The Hazards of Mercury Vapor. *Z. Anorg. Allg. Chem.* **1926**, *39*, 461-466.

[30] Ruta, S.; Hovorka, O.; Huang, P. W.; Wang, K.; Ju, G.; Chantrell, R. First order reversal curves and intrinsic parameter determination for magnetic materials; Limitations of hysteron-based approaches in correlated systems. *Sci. Rep.* **2017**, *7*(1), 45218..

[31] Donnelly, C.; Guizar-Sicairos, M.; Scagnoli, V.; Gliga, S.; Holler, M.; Raabe, J.; Heyderman, L. J. Three-dimensional magnetization structures revealed with X-ray vector nanotomography. *Nature* **2017**, *547*(7663), 328-331.

[32] Donnelly, C.; Metlov, K. L.; Scagnoli, V.; Guizar-Sicairos, M.; Holler, M.; Bingham, N. S.; Raabe, J.; Heyderman, L. J.; Cooper, N. R.; Gliga, S. Experimental observation of vortex rings in a bulk magnet. *Nat. Phys.* **2020**, 17 (3), 316-321.

[33] Rana, A.; Liao, C. T.; Iacocca, E.; Zou, J.; Pham, M.; Lu, X.; Subramanian, E. E. C.; Lo, Y. H.; Ryan, S. A.; Bevis, C. S.; Karl, R. M.; Glaid, A. J.; Rable, J.; Mahale, P.; Hirst, J.; Ostler, T.; Liu, W.; O'Leary, C. M.; Yu, Y. S.; Bustillo, K.; Ohldag, H.; Shapiro, D. A.; Yazdi, S.; Mallouk, T. E.; Osher, S. J.; Kapteyn, H. C.; Crespi, V. H.; Badding, J. V.; Tserkovnyak, Y.; Murnane, M. M.; Miao, J. Three-dimensional topological magnetic monopoles and their interactions in a ferromagnetic meta-lattice. *Nat. Nanotechnol.* **2023**, 18 (3), 227-232.

[34] Miao, J. Computational microscopy with coherent diffractive imaging and ptychography. *Nature* **2025**, 637, 281–295.

[35] Miao, J.; Charalambous, P.; Kirz, J.; Sayre, D. Extending the methodology of X-ray crystallography to allow imaging of micrometre-sized non-crystalline specimens. *Nature* **1999**, 400 (6742), 342-344.

[36] Regan, T. J.; Ohldag, H.; Stamm, C.; Nolting, F.; Lüning, J.; Stöhr, J.; White, R. L. Chemical effects at metal/oxide interfaces studied by x-ray-absorption spectroscopy. *Phys. Rev. B* **2001**, 64(21), 214422.

[37] Maiden, A. M.; Rodenburg, J. M. An improved ptychographical phase retrieval algorithm for diffractive imaging. *Ultramicroscopy* **2009**, 109 (10), 1256-1262.

[38] Scott, M. C.; Chen, C. C.; Mecklenburg, M.; Zhu, C.; Xu, R.; Ercius, P.; Dahmen, U.; Regan, B. C.; Miao, J. Electron tomography at 2.4-angstrom resolution. *Nature* **2012**, 483 (7390), 444-447.

[39] Yang, Y.; Zhou, J.; Zhu, F.; Yuan, Y.; Chang, D.J.; Kim, D. S.; Pham, M.; Rana, A.; Tian, X.; Yao, Y.; Osher, S. J.; Schmid, A. K.; Hu, L.; Ercius, P.; Miao, J. Determining the three-dimensional atomic structure of an amorphous solid. *Nature* **2021**, 592 (7852), 60-64.

[40] Pham, M.; Yuan, Y.; Rana, A.; Osher, S.; Miao, J. Accurate real space iterative reconstruction (RESIRE) algorithm for tomography. *Sci. Rep.* **2023**, 13 (1), 5624.

[41] Pham, M.; Lu, X.; Rana, A.; Osher, S.; Miao, J. Real space iterative reconstruction for vector tomography (RESIRE-V). *Sci. Rep.* **2024**, 14 (1), 9541.

[42] Zang, J.; Cros, V.; Hoffmann, A. *Topology in magnetism. Springer* **2018**, 192.

[43] Zou, J.; Kim, S. K.; Tserkovnyak, Y. Topological transport of vorticity in Heisenberg magnets. *Phys. Rev. B* **2019**, 99 (18), 180402.

[44] Tserkovnyak, Y.; Zou, J.; Kim, S. K.; Takei, S. Quantum hydrodynamics of spin winding. *Phys. Rev. B* **2020**, 102 (22), 224433.

[45] Lepadatu, S. Micromagnetic Monte Carlo method with variable magnetization length based on the Landau–Lifshitz–Bloch equation for computation of large-scale thermodynamic equilibrium states. *J. Appl. Phys*. **2021**, 130 (16), 163902.

[46] Lepadatu, S. Boris computational spintronics—High performance multi-mesh magnetic and spin transport modeling software. *J. Appl. Phys.* **2020**, 128 (24), 243902.

[47] Evans, R. F. L.; Hinzke, D.; Atxitia, U.; Nowak, U.; Chantrell, R. W.; Chubykalo-Fesenko, O. Stochastic form of the Landau-Lifshitz-Bloch equation. *Phys. Rev. B* **2012**, 85 (1), 041133.